Parallel ghost imaging with ultra low dose and high pixel resolution

Nixi Zhao,[1,2,3] Jie Tang,[1,2,3] Changzhe Zhao,[1,2,3] Jianwen Wu,[1,2,3] Han Guo,[2] Haipeng Zhang,[2]* and TiQiao Xiao[1,2,3,*]

[1] *Shanghai Institute of Applied Physics, Chinese Academy of Sciences, Shanghai 201800, People's Republic of China*

[2] *Shanghai Synchrotron Radiation Facility/Zhangjiang Lab, Shanghai Advanced Research Institute, Chinese Academy of Sciences, Shanghai 201204, People's Republic of China*

[3] *University of Chinese Academy of Sciences, Beijing 100049, People's Republic of China*

*tqxiao@sari.ac.cn

*zhanghp@sari.ac.cn

Abstract: Ghost imaging, as a novel imaging technique, enables image acquisition under low-light conditions through single-pixel measurements. It holds tremendous potential across various application areas, such as biomedical imaging, remote sensing, biometrics, astronomy, and three-dimensional imaging. However, reconstructing high-resolution images typically requires a large number of single-pixel samples, which is time-consuming and presents practical limitations for its application. Parallel ghost imaging, wherein each pixel of a position-sensitive detector is used as a bucket detector to perform thousands of measurements in parallel, theoretically allows for high resolution, extra-large field-of-view, and ultra-low dose non-local imaging.

In previous work, we independently achieved three distinct milestones in parallel ghost imaging: first, we realized high pixel resolution, then we demonstrated low-dose imaging, and finally, we successfully implemented ultra-large field-of-view imaging, with each of these advances being accomplished separately and independently. Moreover, we also introduced a global ghost imaging framework specifically designed for bucket detector arrays. In this study, we present two key innovations: First, we implemented low-dose parallel ghost imaging within the computational ghost imaging framework, replacing the crystal beam-splitting method, which significantly improved image quality compared to prior approaches. Second, for the first time, we simultaneously achieved the three exceptional features of high resolution, low dose, and large field-of-view in parallel ghost imaging. In just a few minutes, we were able to generate a ghost image with a resolution of 2016 × 2016 pixels, an effective pixel size of 0.65 micrometers, and an equivalent total exposure time as low as 0.12 ms. In contrast, traditional projection-based imaging requires an exposure time of 500 ms, and the physical limit of high-resolution detectors is 1.004 ms. The total dose in parallel ghost imaging is significantly lower than what is achievable with the shortest exposure time of the detector, effectively reconstructing object information from the "ghost."

We propose this parallel ghost imaging framework, which is expected to pave the way for the practical implementation and commercialization of ghost imaging technology.

1. Introduction

The traditional imaging model primarily consists of three components: the light source, the object, and the optical system. In contrast, ghost imaging (GI), a novel imaging technique, employs a non-localized approach to separate detection from imaging. Ghost imaging involves splitting the light into two beams: one beam carries the object information but lacks resolution, while the other beam carries resolution but lacks object information. Neither beam alone is capable of imaging, but by correlating the two beams computationally, the object information can be reconstructed. Hence, ghost imaging is also referred to as correlation imaging.

Ghost imaging originates from the Hanbury-Brown and Twiss (HBT) experiment [1, 2]. In

1988, Klyshko [3] theoretically proposed a ghost imaging scheme using entangled photon pairs. In 1994, Ribeiro et al. [4] discovered the phenomenon of ghost interference using entangled photon pairs. In 1995, Pittman et al. [5] experimentally demonstrated ghost imaging using entangled photon pairs. In 2002, Bennink et al. [6] realized ghost imaging with classical light sources, proving that entangled light sources are not a necessary condition for ghost imaging. Furthermore, ghost imaging has been shown to be feasible in various fields, including atomic [7], electronic [8], neutron [9, 10], and X-ray [11–15] imaging. In 2008, Shapiro [16] theoretically proposed a computational ghost imaging scheme, making single-channel ghost imaging possible. In 2009, Bromberg et al. [17] experimentally realized computational ghost imaging. In the same year, Katz et al. [18] integrated compressive sensing techniques from image processing with computational ghost imaging, significantly reducing the number of samples required for ghost imaging. This development made dose reduction in X-ray ghost imaging feasible. Moreover, ghost imaging has enormous potential across various application areas, including biomedical imaging [19], remote sensing [20], biometrics [21, 22], astronomy [23], and three-dimensional imaging [24, 25].

However, to reconstruct high-resolution images, Ghost imaging typically requires a large number of single-pixel samples, which poses challenges for its practical application. The concept of parallel ghost imaging (PGI) was introduced by Kingston et al. [9] to address this issue. This method treats each pixel of a position-sensitive detector as an independent bucket detector, enabling the simultaneous execution of tens of thousands of ghost imaging measurements at once. Kingston et al. and Zhang et al. successfully demonstrated PGI in neutron [9] and X-ray [26,27], respectively. Later, O. Sefi et al. extended similar work to high-energy X-rays [28]. However, implementing PGI through artificially fitting bucket detector arrays only validates the feasibility of the concept, and the intrinsic characteristics of PGI—such as large field-of-view, enhanced resolution, and dose reduction—are not inherently realized in these approaches.

To address this issue, we established true magnification between the reference arm and the object arm via a lens, achieving sub-micron level (0.325 μm/pixel) high-pixel resolution parallel ghost imaging, and reducing the experimental time from tens of minutes to just a few minutes. Zhao et al. realized low-dose ghost imaging by employing two detectors in crystal beam-splitter ghost imaging. We achieved extra-large field-of-view ghost imaging by constructing an extremely large speckle space, enabling 14,000 × 10,000 pixel imaging. Additionally, we proposed global ghost imaging(GGI) specifically designed for bucket detector arrays, which allows high-quality reconstruction with an ultra-low sampling rate of just 8 measurements. GGI also effectively eliminates the discontinuities between subsystems in ghost imaging. All the above-mentioned work can only individually realize one of the exceptional features of parallel ghost imaging.

In this work, our innovations are twofold: First, we replaced the crystal beam-splitter framework with a computational ghost imaging framework, which significantly improved the image quality of low-dose parallel ghost imaging compared to previous methods. Second, we combined high resolution with low dose by progressively increasing the magnification of the reference arm, from 2× to 4×, and finally up to 10×. For the first time, we simultaneously realized the three exceptional features of parallel ghost imaging: high resolution, low dose, and large field-of-view. In just a few minutes, we were able to achieve a 2016 × 2016 image with an effective pixel size of 0.65 μm and an equivalent total exposure time as low as 0.12 ms. In contrast, conventional projection imaging requires 500 ms, and the shortest exposure time for high-resolution detectors is 1.004 ms. The total imaging dose in parallel ghost imaging is much lower than the shortest exposure time achievable by the detector, effectively reconstructing the object information literally from the "ghost." We propose this parallel ghost imaging framework, which is expected to pave the way for the practical application and commercialization of ghost imaging.

2. Parallel ghost imaging with ultra low dose

Model For the ghost imaging model from a classical perspective, the bucket detector signals acquired from N measurements in object arm can be written in the form of a matrix in Eq.1.

$$\begin{bmatrix} B_1 \\ B_2 \\ \vdots \\ B_N \end{bmatrix} = \begin{bmatrix} I_1(1,1) & I_1(1,2) & \cdots & I_1(p,1) & \cdots & I_1(p,q) \\ I_2(1,1) & I_2(1,2) & \cdots & I_2(p,1) & \cdots & I_2(p,q) \\ \vdots & \vdots & \vdots & \vdots & \vdots & \vdots \\ I_N(1,1) & I_N(1,2) & \cdots & I_N(p,1) & \cdots & I_N(p,q) \end{bmatrix} \begin{bmatrix} T(1,1) \\ T(1,2) \\ \vdots \\ T(p,q) \end{bmatrix} \tag{1}$$

The object's transmittance function $T(x,y)$, which contains internal structural information of the sample, is the unknown target we aim to reconstruct in ghost imaging. Both the image size of the mask and the reconstructed ghost image of samples are $p \times q$. The transmittance function of the k-th mask is denoted as $I_k(x,y)$, where $x = 1, \cdots, p$ and $y = 1, \cdots, q$, respectively. N represents the number of measurements, B_i denotes the bucket detector signal during the i-th measurement, and the sampling rate is defined as the number of measurements divided by the number of image pixels, i.e. $\frac{N}{p \times q}$. A higher sampling rate leads to higher quality of ghost imaging. For the detector in the object arm, the incident X-ray photons need to pass through the mask and subsequently through the object, which means that the absorption of both the mask and object should be taken into account. Ghost imaging, at its essence, is solving underdetermined linear equation set. PGI simply utilizes this process repeatedly for all the single pixels of the bucket detector array in the object arm, as shown in Fig.1.(b).

Algorithm PGI is based on the Total Variation Augmented Lagrangian Alternating Direction Algorithm [29] using compressive sensing. TVAL3 uses Total Variation Regularization (TV) as an iterative model:

$$\min_u \sum_i \|D_i u\|, \quad s.t. Au = b, \tag{2}$$

A is the speckle patterns, u is the image of the object to be solved, b is the measurements of the bucket detector, $D_i u$ is the gradient of u at pixel i, $\|.\|$ is the $l1$ norm. The Augmented Lagrangian method transforms a constrained model into an unconstrained objective function, and then uses the Alternating Direction method to solve the objective function at high speed.

Experiment We constructed an experimental platform at the Shanghai Synchrotron Radiation Facility BL13HB [30], as depicted in Fig.2.(a). The synchrotron bending magnet emits a beam, which is monochromatized by a double-crystal monochromator. Filters and slits positioned before and after the monochromator filter out stray light and define the beam profile. Prior to reaching the sample, the incident X-ray beam is modulated by a seven-layer 200-mesh sandpaper, providing a randomly modulated light field for the reference beam of ghost imaging.

For PGI to achieve dose reduction, the key lies in the use of two detectors. The detector with high resolution but a long exposure time is referred to as the high-resolution detector, which is placed on the reference arm. Through long-term acquisition, the fine distribution of the speckle pattern can be obtained. The detector with low resolution but a short exposure time is named the high-sensitivity detector, which is placed on the object arm. It can complete the low-resolution acquisition of object information with a dose far lower than that required by conventional projection imaging. Subsequently, the low-resolution and low-dose object signals obtained by the bucket detector array are correlated and calculated with the high-resolution and high-dose speckle information. After introducing compressed sensing, an object image with a
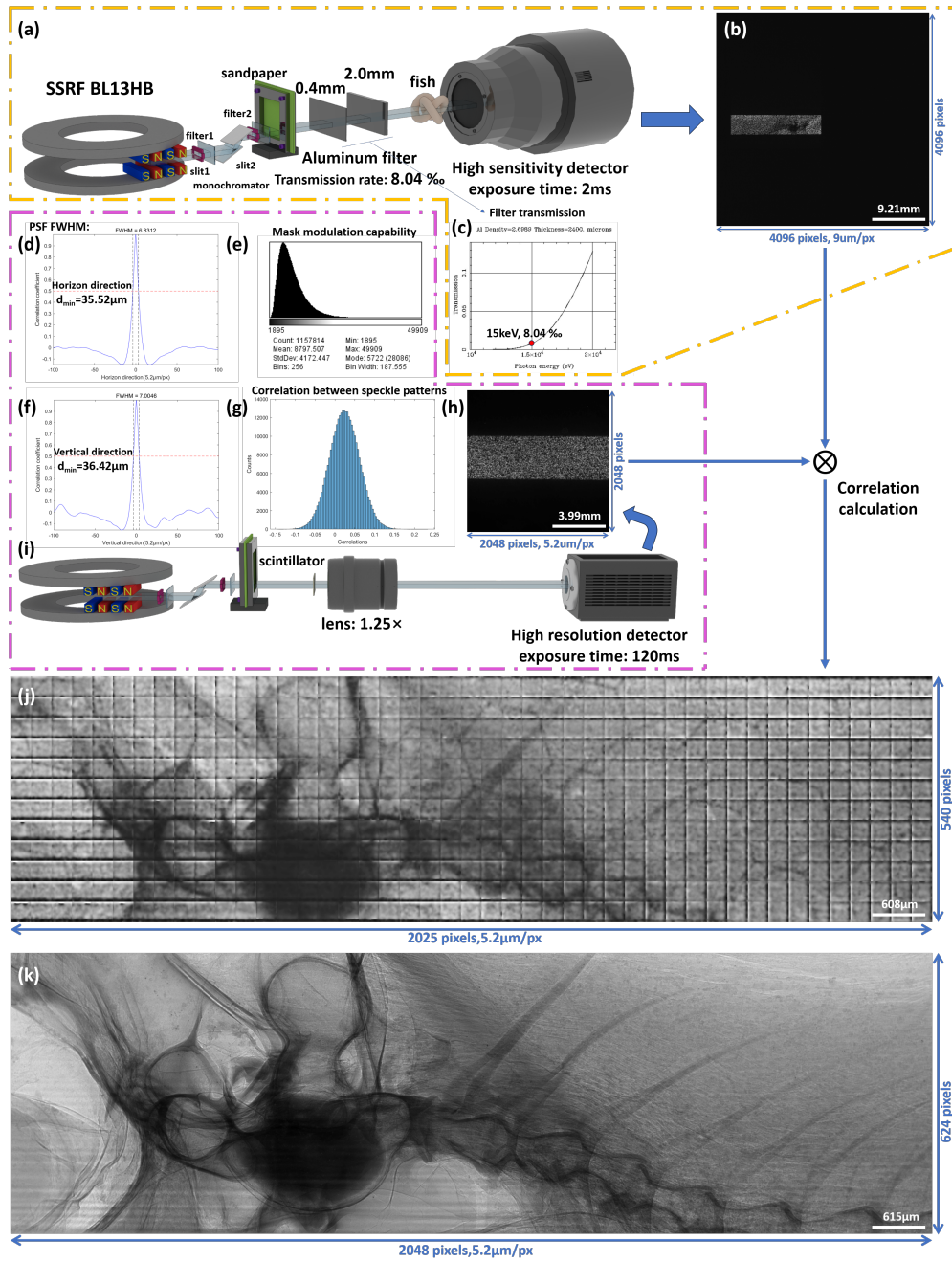
Fig. 1. Parallel ghost imaging with ultra low dose: (a) Schematic diagram of the object arm. (b) Images acquired by the object arm. (c) Attenuation of a 2.4 mm aluminum sheet at 15 keV under different energies. (d, f) Full width at half maximum of the point spread function of the speckle pattern under 1.25× magnification. (e) Modulation capability of the mask under 1.25× magnification. (g) Degree of correlation among speckle patterns under 1.25× magnification. (i) Schematic diagram of the reference arm. (h) Speckle patterns collected by the reference arm. (j) Reconstruction results of parallel ghost imaging, with the number of measurements being 800 and the sampling rate being 39.5%. (k) Standard projection imaging using a high-resolution detector.
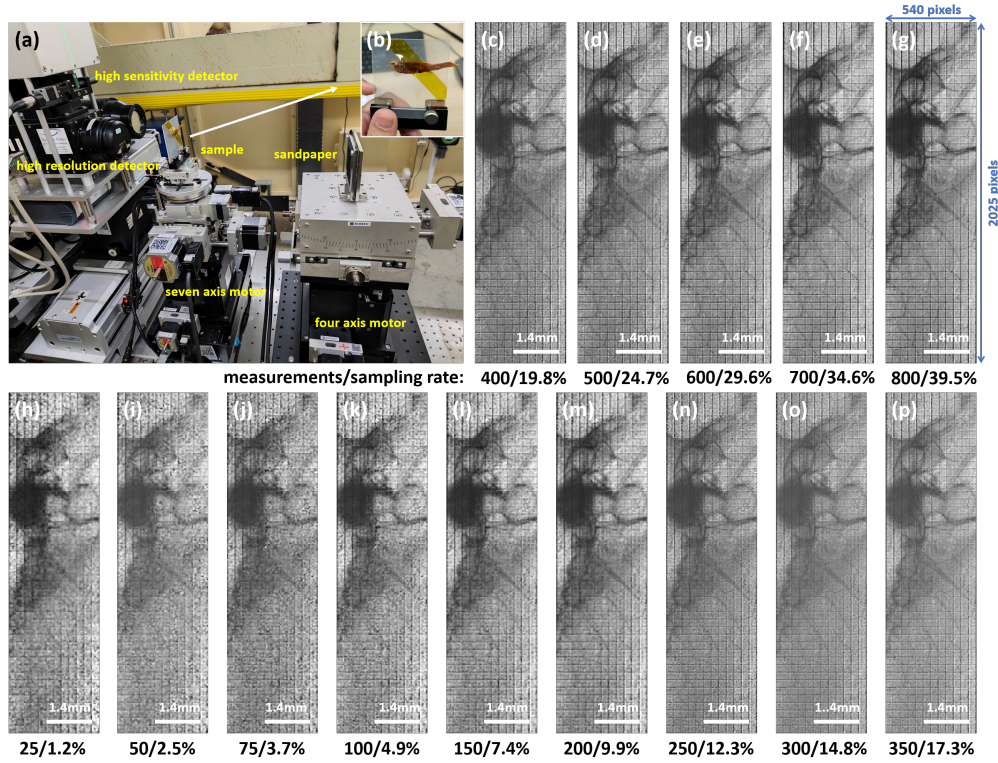
Fig. 2. (a) Diagram of the experimental setup for parallel ghost imaging with ultra low dose. (b) Sample — a fish. A series of reconstruction result images, with the number of measurements/sampling rates being (h) 25/1.2%, (i) 50/2.5%, (j) 75/3.7%, (k) 100/4.9%, (l) 150/7.4%, (m) 200/9.9%, (n) 250/12.3%, (o) 300/14.8%, (p) 350/17.3%, (c) 400/19.8%, (d) 500/24.7%, (e) 600/29.6%, (f) 700/34.6%, and (g) 800/39.5%.

quality close to that of traditional projection imaging but with a dose much lower than that of traditional imaging can be reconstructed.

The product name of the high-sensitivity detector is "X-ray 16.4 MP air cooled sCMOS camera with 52mm input", with a resolution of 4096 × 4096 and a pixel size of 9 μm. Aluminum sheets with a thickness of 2.0 mm and 0.4 mm are placed in front of the high-sensitivity detector to significantly reduce the ionizing radiation dose. When the experimental energy is 15 keV, the 2.4 mm thick aluminum sheet can attenuate the X-ray to 8.04‰ (Fig.1.(c)), that is, the radiation dose is reduced by 124 times. The exposure time of the high-sensitivity detector in the experiment is 2 ms, and the object signal collected is shown in Fig.1.(b). The experimental optical path of the object arm is shown in Fig.1.(a).

The high-resolution imaging system consists of a 100 μm thick scintillation crystal (LuAG:Ce), an optical conversion microscope (model: Optique Peter MICRX016), and an sCMOS detector (Hamamatsu ORCA-Flash 4.0 C11440). The effective area of the detector is 6.6 × 6.6 mm², the pixel size is 6.5 μm, and the number of pixels is 2048 × 2048. We use a 1.25× magnifying lens, with an effective pixel size of 5.2 μm. The exposure time of the high-resolution detector in the experiment is 120 ms. The experimental optical path of the reference arm is shown in Fig.1.(i), and the high-definition speckle pattern it records is shown in Fig.1.(h).

Speckle The speckle pattern has a decisive impact on the reconstruction quality of ghost imaging, because the resolution of the reconstruction result cannot be smaller than the minimum effective feature of the speckle pattern. Generally, with smaller pixels in the reference arm, the detector can capture mask information with a higher density, which means better image quality. With larger pixels in the object arm, the detector can capture the encoded object information more quickly, which implies a lower radiation dose. The effective aperture of 200-mesh sandpaper is approximately 75 μm, which cannot describe the minimum feature of the mask. The irregular edges of the particles, the sharp density gradient changes inside the particles, and the superposition of seven layers of sandpaper all make the minimum effective feature much smaller than the particle width. The modulation ability of the mask on X-rays is shown in Fig.1.(e). The point spread function (PSF), as the auto-covariance of the mask pattern, is the soft upper limit of the resolution of the final imaging result of ghost imaging. However, under a high sampling rate, the PSF may be exceeded. The full width at half maximum (FWHM) of the PSF in the horizontal and vertical directions can be seen in Fig.1.(d) and (f). If a speckle can be represented by the linear superposition of other speckle patterns, it is considered invalid sampling. The statistical histogram of the correlation degree of any two speckle combinations (C^2_{400}) is shown in Fig.1.(g), which means that the random speckles can be approximately regarded as being orthogonal to each other.

Registration Registration has always been a challenge in parallel ghost imaging. When using two detectors, we need refined registration to make the image positions of the reference arm and the object arm correspond one by one. Firstly, we perform a soft summation on the object arm signals with a unit of 26×26 so that they can be perfectly aligned with the 5.2 μm image size of the high-resolution detector without generating errors, thus forming a 45-fold magnification relationship between the object arm and the reference arm($9 \times 26 \div 5.2 = 45$). Then, we leave pixel redundancy around the image. Subsequently, by taking the quality of the reconstructed image as a criterion, we move and register to make the error less than one pixel of the reference arm.

Results Ultimately, we achieved ghost imaging with an image size of 2025×540 and a pixel size of 5.2 μm within a total acquisition time of several minutes. The reconstruction result is shown in Fig.1.(j). The number of acquisitions was 800, with a sampling rate of 39.5%, and the sample was a fish (Fig.2.(b)). The time required for direct projection imaging of the object using the high-resolution detector on the reference arm was 120 ms, as shown in Fig.1.(k). Through actual measurements by the ionization chamber, it was found that in the experiment, the actual dose of each measurement on the object arm was attenuated by 415 times compared to that of traditional projection imaging under the same exposure. The detailed discussion and analysis regarding the equivalent dose conversion will be presented in Section 3.

Based on this, the equivalent exposure times of the reconstruction results for 800 (Fig.2.(g)), 700 (Fig.2.(f)), 600 (Fig.2.(e)), 500 (Fig.2.(d)), 400 (Fig.2.(c)), 350 (Fig.2.(p)), 300 (Fig.2.(o)), 250 (Fig.2.(n)), 200 (Fig.2.(m)), 150 (Fig.2.(l)), 100 (Fig.2.(k)), 75 (Fig.2.(j)), 50 (Fig.2.(i)), and 25 (Fig.2.(h)) acquisitions were 3.85 ms, 3.37 ms, 2.89 ms, 2.40 ms, 1.92 ms, 1.68 ms, 1.44 ms, 1.20 ms, 0.96 ms, 0.72 ms, 0.48 ms, 0.36 ms, 0.24 ms, and 0.12 ms respectively.

It has been demonstrated that ghost imaging can achieve X-ray imaging with an extremely low dose. Regardless of the sampling rate, the dose required for ghost imaging is far less than that for standard imaging (120 ms). The problems that ghost imaging had difficulties in achieving high-quality imaging and that experiments took an extremely long time when there were a large number of measurements have been solved by parallel ghost imaging. Compared with the low-dose parallel ghost imaging achieved through the crystal beam-splitting framework, the low-dose parallel ghost imaging accomplished in this work has significantly improved the image

quality. Moreover, we will go one step further and attempt to simultaneously realize another major characteristic of ghost imaging besides low dose—super-resolution.

3. Parallel ghost imaging with ultra low dose and high pixel resolution

Results In the experiment combining dose reduction and high resolution, the part responsible for low-dose detection does not need to be changed. Therefore, the experimental optical path of the object arm is shown in Fig.3.(a). For the part responsible for high-resolution recording of the speckle pattern, optical lenses are used for magnification to improve the resolution. The magnification multiples gradually increase from 2 × to 4 × and then to 10 ×. The optical lens group is shown in Fig.5.(b). The optical paths of the reference arm corresponding to different magnification multiples are shown in Fig.3.(b, n, z), and the ghost imaging reconstruction results are listed in Fig.3.(d - m, p - y, B - K). A larger fish, the sardina pilchardus, is used as the sample. The traditional projection imaging results after different magnification multiples are listed as standards in Fig.3.(c, o, A). The signals of the bucket detector array collected from the object arm are scaled down so that the magnification multiple of the object arm to the reference arm with three resolutions is 36, and the reduction ratios are 13, 6.5, and 2.6 respectively.

From the experimental results, we can see that as the resolution gradually reaches the sub-micron level, the signal-to-noise ratio of the experimental results gradually decreases. This is because the influences of the minimum feature size of the mask, the movement accuracy of the motor, lens aberration distortion, etc. are magnified along with the increase in resolution. We will continue to work on this in our subsequent work and strive to achieve high resolution rather than high pixel resolution.

Speckles As the resolution gradually increases, a series of phenomena are worthy of discussion. The magnification multiples gradually change from 1.25 ×, 2 ×, 4 × to 10 ×, and the minimum feature resolution of the speckle gradually decreases from 35 μm, 28 μm, 17 μm to 11 μm. This is a powerful proof that lens magnification can achieve super-resolution, as shown in Fig.4.(b - c, g - h, l - m). In addition, another phenomenon has been discovered. As the resolution improves, the uncorrelation between different speckle patterns gradually weakens, which will have an impact on the reconstruction results, as can be seen in Fig.4.(d, i, n).

The modulation ability of the mask is insignificant in simulation experiments and ghost imaging can be achieved by slightly changing the light field. However, in actual experiments, due to the influence of noise, we need the modulation ability to be much greater than the uncertainty brought by the noise, as shown in Fig.4.(e, j, o). In the future, if we want to achieve nanometer-level resolution and centimeter-level field of view, we need to design, customize, screen, and analyze masks specifically suitable for parallel ghost imaging.

Dose The most important discussion regarding X-ray ghost imaging undoubtedly lies in the dose. The optical path diagram of the standard imaging model is shown in Fig.5.(g). In the optical path of the object arm in ghost imaging (Fig.3.(a)), the dose that the object receives less than that in standard imaging during each measurement comes from the attenuation of the sandpaper and the 2.4 mm aluminum sheet. The theoretical attenuation curve of the 2.4 mm thick aluminum sheet for X-rays with different energies is shown in Fig.1.(c). In the experiment, the energy is 15 keV, and the dose is attenuated to 8.04‰ of the original value theoretically. However, this is not rigorous enough. We arranged an ionization chamber (Fig.5.(d)). The current value read out by it has a linear relationship with the radiation dose and can record the changes in X-rays in real time. The aluminum sheet is built inside the vacuum chamber of the optical shed, so it is not present in the experimental shed (Fig.5.(c)). During traditional projection imaging, the current of the ionization chamber is shown in Fig.5.(f), which is 3.23e-5 A. After adding the 2.4 mm aluminum sheet, the current is shown in Fig.5.(h), which is 2.87e-7 A, and the X-ray is
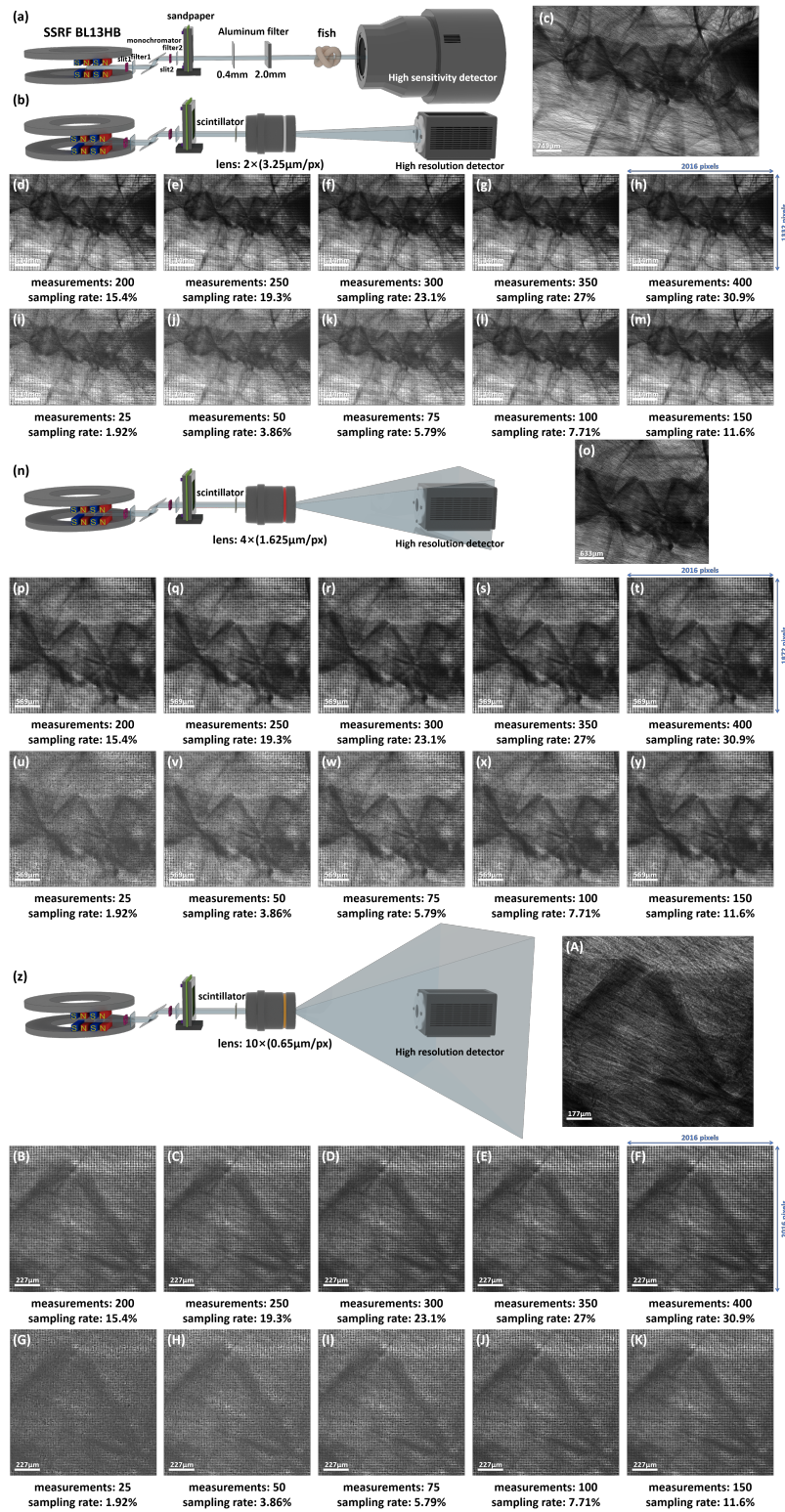
Fig. 3. Parallel ghost imaging with ultra low dose and high pixel resolution: (a) Schematic diagram of the object arm. (b) Reference arm under 2× magnification. (c) Standard projection imaging under 2× magnification. (d - m) Reconstruction result images of ghost imaging under 2× magnification. (n) Reference arm under 4× magnification. (o) Standard projection imaging under 4× magnification. (p - y) Reconstruction result images of ghost imaging under 4× magnification. (z) Reference arm under 10× magnification. (A) Standard projection imaging under 10× magnification. (B - K) Reconstruction result images of ghost imaging under 10× magnification.
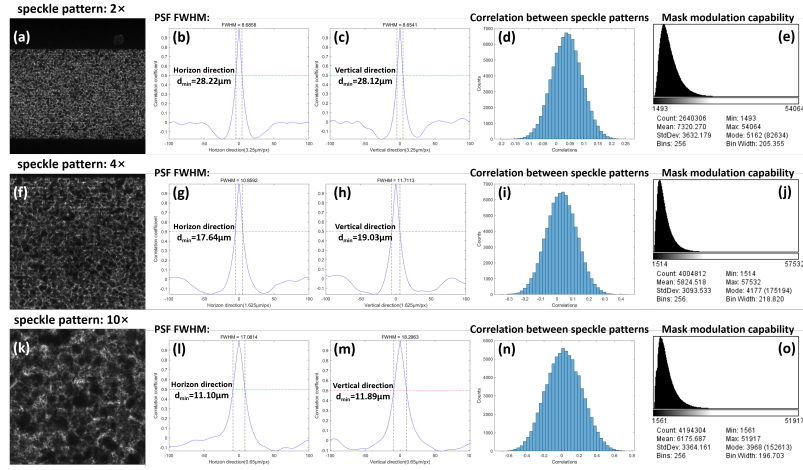
Fig. 4. Analysis of the random speckle modulation under different magnification factors. The speckle patterns at 2× magnification in (a), 4× magnification in (f), and 10× magnification in (k). The point spread function (PSF) of the speckle in the horizontal and vertical directions at 2× magnification in (b - c), 4× magnification in (g - h), and 10× magnification in (l - m). The degree of correlation between speckle patterns at 2× magnification in (d), 4× magnification in (i), and 10× magnification in (n). The modulation ability of the mask at 2× magnification in (e), 4× magnification in (j), and 10× magnification in (o).

attenuated to 8.88‰, or in other words, the dose of each measurement is reduced by 112 times. The experimental attenuation ratio of the aluminum sheet is different from the theoretical value, so real-time observation by the ionization chamber is necessary. The sandpaper modulates the X-rays, and its attenuation of the X-rays cannot be ignored. Placing the mask between the ionization chamber and the light exit port (Fig. 5.(i)) can achieve the measurement of the attenuation ability of the mask, as shown in Fig. 5.(j). The current of the ionization chamber for the total attenuation of the X-rays by the 2.4 mm aluminum sheet and the sandpaper is 7.79e-8 A, and the dose will be 2.4‰ of the original value, that is, the dose is reduced by 415 times, as shown in Fig. 5.(k).

Traditional projection imaging		Parallel ghost imaging (measurements	sampling rate)								
Magnification	Dose (exposure time)	25(1.92%)	50(3.86%)	75(5.79%)	100(7.71%)	150(11.6%)	200(15.4%)	250(19.3%)	300(23.1%)	350(27%)	400(30.9%)
2×	250ms	0.12ms	0.24ms	0.36ms	0.48ms	0.72ms	0.96ms	1.2ms	1.44ms	1.68ms	1.92ms
4×	3s	0.12ms	0.24ms	0.36ms	0.48ms	0.72ms	0.96ms	1.2ms	1.44ms	1.68ms	1.92ms
10×	500ms	0.12ms	0.24ms	0.36ms	0.48ms	0.72ms	0.96ms	1.2ms	1.44ms	1.68ms	1.92ms

Table 1. Dose comparison between traditional projection imaging and parallel ghost imaging at different numbers of measurements and different magnification factors.

This means that the total exposure time of the object arm measurement can be equivalently converted to the exposure time of conventional projection imaging by shortening it by 415 times. The equivalent exposure times of parallel ghost imaging at different numbers of measurements are listed on the right side of Table.1, and the exposure times required for traditional projection imaging are listed on the left side of Table.1. By comparison, we can see that a huge dose reduction has been achieved, and the problems that have long existed in the field of ghost imaging, such as low resolution, poor image quality, a large number of measurements, and long experiment duration, have also been solved by the parallel ghost imaging architecture.

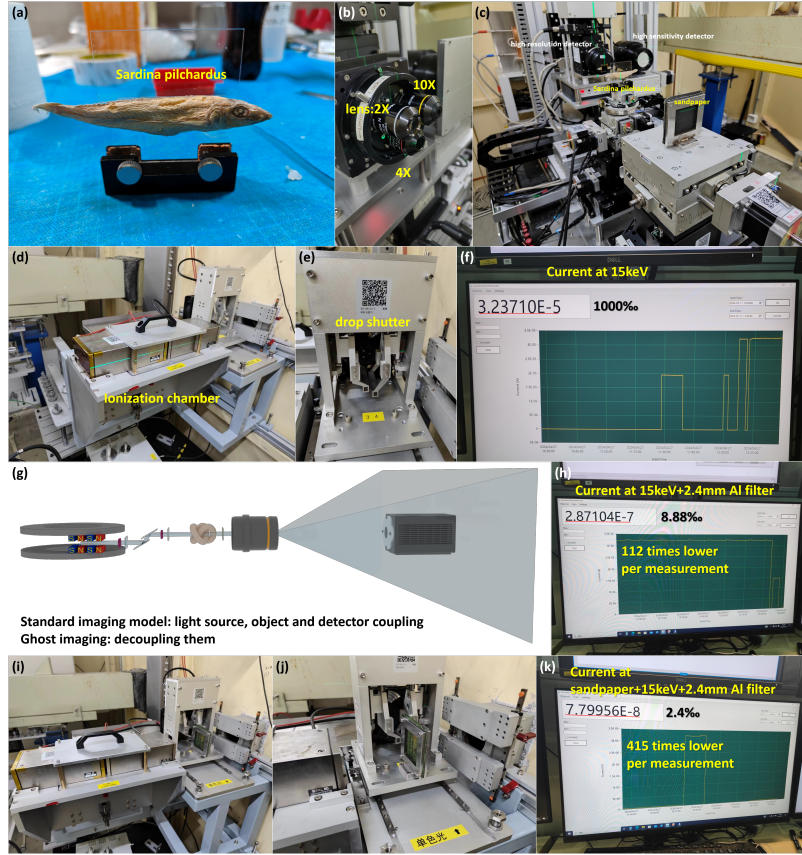Furthermore, the physically shortest exposure time that can be achieved by the high-resolution

Fig. 5. Discussion on the dose of parallel ghost imaging. (a) Sample — sardine pilchardus. (b) Optical lens groups — 2×, 4×, 10×. (c) Experimental setup for parallel ghost imaging with high resolution, low dose and large field of view. (d) Ionization chamber, used for dose measurement. (e) Shutter, if used, can shield the exposure during the movement of the motor. (f) Dose of standard imaging. (g) Standard imaging model. (h) True attenuation of the dose by a 2.4 mm aluminum sheet. (i, j) Dose measurements for the mask. (k) True dose per measurement of ghost imaging with a 2.4 mm aluminum sheet plus the mask.

detector is 1.004 ms, and the minimum dose achieved by parallel ghost imaging is much lower than this. This means that the object information has been reconstructed from the "ghost", which is impossible to achieve with traditional standard imaging. The total duration of the experiment is several minutes, and most of the time is consumed in the movement of the mask. If we want to eliminate the dose during this part, we can use a shutter to block the light beam when the mask is moving. The shutter is shown in Fig. 5.(e).

4. Conclusion

All in all, after achieving high-resolution and low-dose parallel ghost imaging respectively, we first significantly improved the image quality of low-dose parallel ghost imaging and then combined the two. Eventually, for the first time in the world, we were able to achieve ghost imaging with high pixel resolution, a large field of view, and a low dose within an extremely short period of time. We proposed the parallel ghost imaging framework and believe that it will point the way for the practical application and commercialization of ghost imaging.

However, there are still numerous problems in parallel ghost imaging that urgently need to be solved. Although parallel ghost imaging has achieved great breakthroughs, it is still far from the goals that can be theoretically achieved by parallel ghost imaging. There is still huge room for improvement regarding resolution, and we will work hard towards this. Currently, parallel ghost imaging relies on the shanghai synchrotron radiation facility. In order to popularize it, we need to make parallel ghost imaging feasible even with many inexpensive and portable X-ray sources that have poor motor movement accuracy, continuous X-ray energy, and incomplete supporting equipment. Next, we will make efforts in this regard and attempt to prove that parallel ghost imaging is both feasible and has excellent effects on any equipment.

Disclosures. The authors declare no conflicts of interest.

Data Availability Statement. Data underlying the results presented in this paper are not publicly available at this time but may be obtained from the authors upon reasonable request.

References

1. R. Hanbury Brown and R. Q. Twiss, "A test of a new type of stellar interferometer on sirius," in *A Source Book in Astronomy and Astrophysics, 1900–1975,* (Harvard University Press, 1979), pp. 8–12.
2. R. H. Brown and R. Q. Twiss, "Correlation between photons in two coherent beams of light," Nature **177**, 27–29 (1956).
3. D. Klyshko, "Two-photon light: influence of filtration and a new possible epr experiment," Phys. Lett. A **128**, 133–137 (1988).
4. P. S. Ribeiro, S. Pádua, J. M. Da Silva, and G. Barbosa, "Controlling the degree of visibility of young's fringes with photon coincidence measurements," Phys. Rev. A **49**, 4176 (1994).
5. T. B. Pittman, Y. Shih, D. Strekalov, and A. V. Sergienko, "Optical imaging by means of two-photon quantum entanglement," Phys. Rev. A **52**, R3429 (1995).
6. R. S. Bennink, S. J. Bentley, and R. W. Boyd, ""two-photon" coincidence imaging with a classical source," Phys. review letters **89**, 113601 (2002).
7. R. I. Khakimov, B. Henson, D. Shin, *et al.*, "Ghost imaging with atoms," Nature **540**, 100–103 (2016).
8. S. Li, F. Cropp, K. Kabra, *et al.*, "Electron ghost imaging," Phys. review letters **121**, 114801 (2018).
9. A. M. Kingston, G. R. Myers, D. Pelliccia, *et al.*, "Neutron ghost imaging," Phys. Rev. A **101**, 053844 (2020).
10. Y.-H. He, Y.-Y. Huang, Z.-R. Zeng, *et al.*, "Single-pixel imaging with neutrons," Sci. Bull. **66**, 133–138 (2021).
11. H. Yu, R. Lu, S. Han, *et al.*, "Fourier-transform ghost imaging with hard x rays," Phys. review letters **117**, 113901 (2016).

12. D. Pelliccia, A. Rack, M. Scheel, *et al.*, "Experimental x-ray ghost imaging," Phys. review letters **117**, 113902 (2016).
13. A. Schori and S. Shwartz, "X-ray ghost imaging with a laboratory source," Opt. express **25**, 14822–14828 (2017).
14. D. Pelliccia, M. P. Olbinado, A. Rack, *et al.*, "Towards a practical implementation of x-ray ghost imaging with synchrotron light," IUCrJ **5**, 428–438 (2018).
15. A. Schori, D. Borodin, K. Tamasaku, and S. Shwartz, "Ghost imaging with paired x-ray photons," Phys. Rev. A **97**, 063804 (2018).
16. J. H. Shapiro, "Computational ghost imaging," Phys. Rev. A—Atomic, Mol. Opt. Phys. **78**, 061802 (2008).
17. Y. Bromberg, O. Katz, and Y. Silberberg, "Ghost imaging with a single detector," Phys. Rev. A—Atomic, Mol. Opt. Phys. **79**, 053840 (2009).
18. O. Katz, Y. Bromberg, and Y. Silberberg, "Compressive ghost imaging," Appl. Phys. Lett. **95** (2009).
19. Q.-B. Lu, L. Ding, Y.-Y. Zhou, *et al.*, "Ultrasonic holographic ghost imaging," Phys. Rev. Appl. **17**, 034052 (2022).
20. B. I. Erkmen, "Computational ghost imaging for remote sensing," JOSA A **29**, 782–789 (2012).
21. F. Lin, L. Hong, H. Guo, *et al.*, "Ghost identification for qr codes and fingerprints with thermal light modulation," Phys. Rev. Appl. **18**, 054060 (2022).
22. S. Yuan, D. Chen, X. Liu, and X. Zhou, "Optical encryption based on biometrics and single-pixel imaging with random orthogonal modulation," Opt. Commun. **522**, 128643 (2022).
23. D. V. Strekalov, B. I. Erkmen, and N. Yu, "Ghost imaging of space objects," in *Journal of Physics: Conference Series,* vol. 414 (IOP Publishing, 2013), p. 012037.
24. A. M. Kingston, D. Pelliccia, A. Rack, *et al.*, "Ghost tomography," Optica **5**, 1516–1520 (2018).
25. A. M. Kingston, G. R. Myers, D. Pelliccia, *et al.*, "X-ray ghost-tomography: Artefacts, dose distribution, and mask considerations," IEEE Trans. on Comput. Imaging **5**, 136–149 (2018).
26. H. Zhang, K. Li, F. Wang, *et al.*, "Megapixel x-ray ghost imaging with a binned detector in the object arm," Chin. Opt. Lett. **20**, 033401 (2022).
27. C.-Z. Zhao, H.-P. Zhang, J. Tang, *et al.*, "X-ray ghost imaging with a specially developed beam splitter," Synchrotron Radiat. **31** (2024).
28. O. Sefi, A. Ben Yehuda, Y. Klein, *et al.*, "20 µm resolution multipixel ghost imaging with high-energy x-rays," Opt. Express **32**, 37001–37010 (2024).
29. C. Li, W. Yin, H. Jiang, and Y. Zhang, "An efficient augmented lagrangian method with applications to total variation minimization," Comput. Optim. Appl. **56**, 507–530 (2013).
30. J.-F. Ji, H. Guo, Y.-L. Xue, *et al.*, "The new x-ray imaging and biomedical application beamline bl13hb at ssrf," Nucl. Sci. Tech. **34**, 197 (2023).